Improvements in dielectric, electrical and magnetic contributions in $Ca_{0.5}Co_{0.5}Cr_xFe_{2-x}O_4$ spinel ferrites by the substitution of Cr^{3+} ions

Muhammad Imran Arshad[1,2,3*], Hira Zahid[3], Tariq Sajjad[4], Le Duc Tung[1], N. Amin[3], Nguyen Thi Kim Thanh[1,2**], Mongi Amami[5], N. Morley[6], Faisal Alresheedi[7], Afeefa Dastgir[3], Saifeldin M. Siddeeg[5], M. S. Hasan[8***]

[1]*Biophysics Group, Department of Physics and Astronomy, University College London, Gower Street, London, WC1E 6BT, UK.*

[2]*UCL Healthcare Biomagnetic and Nanomaterials Laboratories, 21 Albemarle Street, London W1S 4BS, UK*

[3]*Department of Physics, Govt. College University Faisalabad, 38000, Pakistan.*

[4]*London Center for Energy (LCEE), School of Engineering, London South Bank University, 103 Borough Road, London, SE1 OAA, UK*

[5]*Department of Chemistry, College of Sciences, King Khalid University, \P.O Box 9000, 61413 Abha, Saudi Arabia*

[6]*Department of Materials Science and Engineering, The University of Sheffield, UK, S1 3JD.*

[7]*Department of Physics, College of Science, Qassim University, Buraidah 51452, Saudi Arabia.*

[8]*Department of Physics, The University of Lahore, 53700, Pakistan*

Corresponding author(s)

email: *miarshadgcuf@gmail.com; Mobile no. +923016941617

email: **ntk.thanh@ucl.ac.uk; Mobile no. +44 (0) 207-491-6509

email: ***m.sajjadhasan@hotmail.com; Mobile no. +923334353225

Abstract

In present research, we employed sol-gel auto-combustion method to synthesize soft ferrites, specifically $Ca_{0.5}Co_{0.5}Cr_xFe_{2-x}O_4$, with Cr^{3+} doping, where, x = 0.0, 0.1, 0.2, 0.3, 0.4, 0.5. As the Cr^{3+} concentration increased, we observed decrease in both the average crystallite size (16.4-13.5 nm) and lattice constant (8.3-8.2 Å). Notably, $Ca_{0.5}Co_{0.5}Cr_{0.3}Fe_{1.7}O_4$ sample exhibited the highest AC conductivity at room temperature. Raman spectroscopy confirmed the presence of five active molecular vibrational modes, namely A_{1g}, E_g, and $3T_{2g}$. DC resistivity decreased with the increasing concentration of Cr^{3+}, and the $Ca_{0.5}Co_{0.5}Fe_2O_4$ sample displayed the maximum DC resistivity (6.81×10^8 ohm-cm) at 383 K Curie temperature. Magnetic properties of soft ferrites were characterized through M-H loop analysis, revealing coercivity values in the range of H_C = 1242.6-660.8 Oe. These synthesized ferrites exhibit potential applications in longitudinal recording media owing to their performance in the microwave frequency range (6.0–13 GHz), consistent DC resistivity, and stable dielectric constant.

Keywords: Cr^{3+} doping; Dielectric materials; Raman modes; Electrical Conductivity; Magnetic properties;

1. Introduction

Ferrites have attracted great interest due to their importance in several applications ranging from microwave to radio frequencies [1-4]. Various methods have been employed for synthesizing ferrites; however, the sol-gel auto-combustion route has proven to be economical, free of impurities, and easy to handle [5-7]. This process involves the exothermic reaction of precursor chemicals, resulting in the formation of fine powders with a controlled composition. Its self-sustaining nature eliminates the need for complex equipment and high-temperature processes. Additionally, it enables the synthesis of materials with a homogeneous composition and desirable properties, making it a cost-effective and environmentally friendly approach for producing a wide range of nanoparticles [8]. Nanoferrites with combinations of cations such as Ca, Co, Cr, Ca-Co, Co-Cr, and Ca-Cr have been reported [9-16]. However, there are limited reports on Ca-Co-Cr ferrites. The investigations have been comprehensive, covering various aspects such as material synthesis and characterization, structural and morphological analysis, magnetic properties, and applications. Additionally, attention has been given to the examination of physical, electrical, dielectric, and optical properties. Cobalt ferrite serves as a compelling parent system due to its combination of magnetic properties, electrical resistivity, thermal stability, and adaptability through doping. These characteristics make it a suitable starting point for the development of materials with tailored properties for a wide range of technological applications. The incorporation of Ca and Cr into cobalt ferrites has been demonstrated to enhance both dielectric and magnetic properties, making them suitable for applications in memory devices, recording media, and high-frequency applications. In a study conducted by S. Gowreesan *et al.*(2018), it was noted that the CaCo ferrites exhibit frequency-dependent dielectric dispersion behavior within a frequency range of 50 Hz to 5 MHz. Their observation indicates that $Co_{0.85}Ca_{0.15}Fe_2O_4$ displays promising

characteristics for high-frequency applications, including a high dielectric constant, minimal dielectric losses, and a saturation magnetization of 43.17 emu/g. S. Gowreesan *et al.* (2018) synthesized the Ca-Co ferrites by the application of the self-combustion process and observed a decrease in saturation magnetization from 63.92 to 43.17 emu/g [17]. Rajnish Kumar *et al.* (2016) also prepared the Ca-Co ferrites by using the sol-gel procedure and observed the maximum saturation magnetization for 1.0% doping of Ca [18]. Meanwhile the transition metal Cr^{3+} demonstrates a paramagnetic nature, and its addition can significantly enhance high-frequency performance. This feature makes cobalt and calcium ferrites suitable for GHz-range applications, including microwave devices. In a study by Sika Sarmah *et al.,*(2023), impedance analysis of Cr-substituted cobalt ferrites was performed within the frequency range of 20 Hz to 1 MHz. The materials investigated in this study exhibit promising characteristics for high-frequency applications, showcasing a saturation magnetization of 74.1 emu/g, a high dielectric constant, and a low dielectric loss factor, particularly for the composition $CoFe_{1.98}Cr_{0.02}O_4$ [19]. A series of $CoFe_2O_4$ and $CoCr_{0.9}Fe_{1.1}O_4$ samples were prepared by M. Raghasudha *et al.,*(2016) using the citrate gel chemical method. Notably, the $CoCr_{0.9}Fe_{1.1}O_4$ ferrite sample exhibited decreased coercivity, making it useful for high-frequency transformers applications [13]. Furthermore, in a study conducted by Zahid *et al*.,(2021), Ca-Cr nanoferrites were synthesized using the sol-gel auto-combustion process. The investigation focused on analyzing their structural characteristics, dielectric properties, and the behavior of Ca-Cr ferrites [15]. Ca-Co ferrites are employed as a parent system in various applications due to their unique magnetic and electrical properties, which can be tailored by introducing Cr^{3+} metal ions into the crystal lattice.

In the current research work, we have achieved a frequency range of 6–13 GHz. Cr^{3+} doping exhibits low hysteresis and eddy current losses, which are crucial for efficient operation in

transformers and other electromagnetic devices. For the development of new materials, cation sharing plays an imperative role; thus, the authors also aim to propose the cation distribution of synthesized ferrites. The purpose of the current study is to scientifically observe the different characteristics of Cr-exchanged Ca-Co ferrites. Here, we have synthesized $Ca_{0.5}Co_{0.5}Cr_xFe_{2-x}O_4$ ($0.0 \leq x \leq 0.5$) soft ferrites (*CCCF-soft ferrites*) via the sol-gel auto-combustion method. The sol-gel auto-combustion method is relatively low-cost as compared to other synthesis techniques. The sol-gel auto-combustion process allows for precise control over the formation of the material, resulting in a high-purity product. It is relatively simple to perform and does not require specialized training or extensive experience. Also, it can be used to synthesize a wide range of materials, including ceramics, metal oxides, and composite materials. The composed *CCCF-soft ferrites* were then characterized to explore structural, morphological, electrical, molecular vibrational, dielectric, and magnetic properties.

2. Synthesis and characterizations

2.1 Used materials and synthesis process

The pure analytical reagent (AR) grade compounds were employed as starting materials, such as calcium tetrahydrate [$Ca(NO_3)_2.4H_2O$], chromium Nonahydrate [$Cr(NO_3)_3.9H_2O$], cobalt nitrate hexahydrate [$Co(NO_3)_2.6H_2O$], iron nitrate Nonahydrate [$Fe(NO_3)_3.9H_2O$], and citric acid ($C_6H_8O_7$), to synthesize chromium doped Ca-Co ferrites. The molar ratio of metal nitrates to aqueous citric acid solution was 1:1. The solution was magnetically stirred at 50 revs/min. The chemical reaction for the successful product is: $0.5[Ca(NO_3)_2.4H_2O] + 0.5[Co(NO_3)_2.6H_2O] + x[Cr(NO_3)_3.9H_2O] + (2-x)[Fe(NO_3)_3.9H_2O] \rightarrow Ca_{0.5}Co_{0.5}Cr_xFe_{2-x}O_4$ where (x = 0.0, 0.1, 0.2, 0.3,

0.4 and 0.5). Ammonia solution was added to adjust the pH to 7, creating a neutral or slightly basic environment for the combustion reaction, and the temperature was maintained at 80°C during the process. Initially, the material transformed into a gel and then underwent auto-combustion to transform into a powder. Finally, the obtained ashes were calcined at 600°C (873K) for 8 hours. All necessary safety measures were taken to eliminate any exposure to hazardous substances. The graphical representation of the procedure is shown in Fig 1.

2.2 Characterization techniques

X-ray diffractometer (XRD) Bruker, Model D8 Advance, using filtered copper Kα radiation with wavelength = 1.5 Å used to identify and determination of different crystalline phases of as-prepared powder samples. SEM, NOVA NANOSEM series 450 was utilized to examine surface morphology along with particle size, particle size distribution, shapes, roughness, homogeneity, and porosity level of ferrites. Keithley, Model 2401 source meter, current/voltage/Resistance/Voltage Meter (IV Measurement Meter) two probe was used to measure the electrical properties. Dielectric parameters were determined by IM3533 LCR meter and Impedance Analyzer (IA) at room temperature. RAMAN analysis is used to analyze vibrational modes by using Morphology 4-ID with a 532.8 nm laser excitation. Magnetic properties were revealed by using the vibrating sample magnetometer (VSM-175) in the range of 5000 Oe at room temperature.

3. Results and discussions

Experimental results of *CCCF-soft ferrites* prepared by the sol-gel auto-combustion method are obtained using different characterization techniques. The details are explained in the given parts below.

3.1 Structural Analysis

X-ray diffraction patterns of synthesized *CCCF-soft ferrites* via the sol-gel method are shown in Fig. 2. XRD patterns revealed that the five most prominent peaks (220), (311), (400), (422), and (511) are observed, verifying the development of a single-phase structure. The most intense peak (311) is used to calculate different crystallographic parameters which are given in Table 1. According to XRD data, the crystallite size [20] was calculated as,

$$D = \frac{K\lambda}{\beta \cos\theta} \qquad (1)$$

Where, λ is the wavelength of the X-ray source, K (0.9) is the shape factor and β is FWHM (degree) [21]. Crystallite size was observed in the range of 13.5-16.4 nm as represented in Table 1. By increasing chromium concentration, the crystallite size decreases due to substituent ions that inhibit the growth rate. The value D<50nm is appropriate for the signal-to-noise ratio in the high-density recording media [22]. The annealing process at elevated temperatures typically results in grain sizes exceeding 50 nm, thereby restricting the attainability of ultrafine particles suitable for specific applications, particularly fundamental research. Additionally, it has been observed that the saturation magnetization of magnetic materials decreases as the particle size decreases, thereby imposing limitations on the use of nanosized magnetic materials in magnetic recording [23]. The

presence of non-magnetic layers on the surfaces of fine particles and a fraction of particles within the superparamagnetic range have been proposed as factors contributing to the reduction in saturation magnetization in nanosized magnetic materials [24]. Table 1 represents the crystallite size with increasing chromium concentration. The experimental lattice constant (a_{exp}) and interplanar spacing (d) were investigated by employing Bragg's equation [25] as,

$$a = d_{hkl}\sqrt{(h^2 + k^2 + l^2)} \quad (2)$$

$$\mathrm{d} = \frac{\lambda}{2sin\theta} \quad (3)$$

With the increase of Cr^{3+} ions in Ca-Co nano-ferrites, the lattice constant (a_{exp}) decreased linearly, indicating that the system follows Vegard's law [12]. The dislocation line density increased with the rising chromium concentration. The reduction in lattice constant by increasing chromium concentration is correlated to the dissimilarity in ionic radii of Fe^{3+} (0.645 Å) and Cr^{3+} (0.615 Å), as given in Table 1. Similar trends have been reported by Mehmat Kuru *et al.,* [26]. Additionally, the addition of Cr^{3+} ions may reduce intrinsic stress and shrink the unit cell of the spinel structure by decreasing lattice distortions. Similar results are also discussed in the literature [27].

Table 1 represents the a_{exp} against the concentration (x) of *CCCF-soft ferrites*. Fig. 3 shows the Rietveld refinement method for the XRD patterns of *CCCF-soft ferrites*. The presence of Fd-3m group is confirmed by this method. The weighted profile factor (R_{wp}) and expected factor (R_{exp}) are named R-factors. The R-factors are employed to confirm the refinement's reliability as illustrated in Table 1. The goodness of fit is also given in Table 1. The lattice constant (a) determined from the Rietveld refinement decreased from 8.3961 Å to 8.3766 Å as given in Table

1. $V=a^3$ [28] is used for unit cell volume for synthesized ferrites are also given in Table 1. The X-ray density (ρ_x) [29] and bulk density (ρ_b) [30] were determined as,

$$\rho_x = \frac{8M}{N_A a^3} \quad (4)$$

$$\rho_b = \frac{m}{\pi r^2 h} \quad (5)$$

Where N_A represents Avogadro's number, M shows molecular weight and "a" represents lattice constant [31]. Calculated values of X-ray and bulk densities are illustrated in Table 1. The X-ray density increased from 5.0 to 5.1 g/cm^3 with the increase in chromium concentration due to the molar mass difference between Cr^{3+} and Fe^{3+} [9]. From Table 1 it can be revealed that $\rho_x > \rho_b$, such behavior is attributed to the appearance of some unnecessary pores during the sintering and synthesizing procedure [32]. Hopping lengths (H_A and H_B) in magnetic ions at A & B sites were measured as [33],

$$H_A = \frac{\sqrt{3}}{4} a \quad (6)$$

$$H_B = \frac{\sqrt{2}}{4} a \quad (7)$$

Table 2 indicates that both H_A and H_B are decreasing with the increasing concentration of Cr^{3+} as both parameters are associated with the lattice constant. Such a decreasing trend reveals a smaller amount of energy is required to shift the charge carriers between cationic sites. Such performance is justified by the Polaron radius $\gamma_p = \frac{1}{2}\left(\sqrt[3]{\frac{\pi a}{6N'}}\right)$ [34] where a is lattice constant and $N' = 96/a^3$ as given in Table 2. With the increasing dopant Cr^{3+}, the value of the polaron radius decreased, and the strain value increased, resulting in an enhanced surface area. The packing factor also decreased

with the increasing chromium substituent, possibly due to the difference in radii between chromium and iron. Various mechanical parameters have been calculated and are illustrated in Table 2. Ionic radii of both sites (r_A, r_B) were calculated with the help of the following relations.

$$r_A = [C_{ACa}.r(Ca^{2+}) + C_{ACo}.r(Co^{2+}) + C_{AFe}.r(Fe^{3+})] \quad (8)$$

$$r_B = \frac{1}{2}[C_{BCo}.r(Co^{2+}) + C_{BCr}.r(Cr^{3+}) + C_{BFe}.r(Fe^{3+})]O_4 \quad (9)$$

Where, C_{Ca}, C_{Co}, $C_{Cr,}$ and C_{Fe} represent the concentration of calcium, chromium, cobalt, and iron, respectively and r represents the ionic radii of elements taken from the cationic distribution. XRD data can be analyzed theoretically with the help of ionic radii and compositions. The present study consists of *CCCF-soft ferrites* in which Cr^{+3} occupies octahedral site [35], Co^{2+} has a partially inverse nature and occupies both octahedral (80%) and tetrahedral (20%) sites [36], Ca^{2+} has a normal nature and occupies tetrahedral site [37]. The ionic radii of Ca^{2+}(0.99Å), Cr^{3+}(0.61Å), Co^{2+}(0.58Å at A site and 0.74Å at B site), Fe^{3+}(0.49Å) at A site and 0.645Å at B site) [38].

Cationic distributions for *CCCF-soft ferrites* are tabulated in Table 3. The value of r_A remains the same and r_B increases, (as given in Table 4) with increasing chromium concentration which indicates the expansion in the octahedral site by doping of chromium. The relation of ionic radii of both sides with concentration is shown in Table 4. By using the ionic radii, the theoretical values of lattice constant (a_{th}) were studied as [4],

$$a_{th}=8/3\sqrt{3}[(r_A+r_o)+\sqrt{3}(r_B+r_o)] \quad (10)$$

Where r_o is the radius of oxygen ions. a_{th} results are tabulated in Table 4, which shows the a_{th} increases with the addition of chromium ions. Furthermore, the oxygen ion parameter (U) has been calculated according to the following relation [39].

$$U = (r_{A+}r_o)\frac{1}{\sqrt{3}a} + \frac{1}{4} \qquad (11)$$

The value of the oxygen ion parameter for the ideal spinel structure is 0.375Å and our values are slightly greater than the ideal value. The calculated "U" was found to be in the range of 0.3 Å, as shown in Table 4, which may occur due to anion displacement from the ideal position. The same trend was also reported by A.A. Birajdar *et al.,* [35]. The reduction in the "U" parameter is a direct result of diminishing the trigonal distortion within the tetrahedral oxygen coordination. As the substitution of Cr ions into the B-sublattice increases at the expense of Fe ions, the number of oxygen vacancies decreases. This change is evident in the decrease observed in the values of the oxygen positional parameter upon introducing Cr substitution [36]. For spinel structure, the tolerance factor (T) was found as [39],

$$T = \frac{1}{\sqrt{3}}\left(\frac{r_A+r_0}{r_B+r_0}\right) + \frac{1}{\sqrt{2}}\left(\frac{r_0}{r_A+r_0}\right) \qquad (12)$$

In the case of ideal soft ferrites, the tolerance factor must be close to unity. In the present research work, the tolerance factor was observed in the range of 1.0 Å, as given in Table 4. It is noticed that "T" is decreasing with the increasing chromium concentration, suggesting the formation of a defect-free spinel ferrite structure [40]. The distances between A-site cations and oxygen ions (R_A) and the distances between B-site cations and oxygen ions (R_B) are examined using the formulas as follows [31],

$$R_A = a/\sqrt{3}\,(\Delta + \tfrac{1}{8}) \quad (13)$$

$$R_B = a\sqrt{3\Delta^2 + {}^{\Delta}/_{2} + \tfrac{1}{16}} \quad (14)$$

In above relation, $\Delta = U_{cal} - U_{ideal}$ represents deviation of the ideal oxygen ion parameter. The calculated bond lengths are tabulated in Table 4. Interatomic distances i.e. tetrahedral edge length (R_x), shared octahedral edge length (R_x') and unshared octahedral edge length (R_x'') [41] are determined by using the equations given below and values represented in Table 4.

$$R_x = \sqrt{2}\left(2u - \tfrac{1}{2}\right)a \quad (15)$$

$$R_X' = \sqrt{2}(1 - 2u)a \quad (16)$$

$$R_X'' = \left(\sqrt{4u^2 - 3u + \tfrac{11}{16}}\right)a \quad (17)$$

All parameters illustrated in equations (13) to (17) are directly associated with the lattice constant. The lattice constant is decreasing with the increase of Cr^{3+} concentration. Hence this factor leads to a decrease in all the parameters given in equations (13) to (17).

3.2 Surface morphological analysis

Scanning electron microscope (SEM) images give information on the particle size, shape, particle size distribution, roughness, porosity, and homogeneity level of ferrites. The SEM images of *CCCF-soft ferrites* at (5.0 μm) resolution are represented in Fig. 4. The synthesized sample has a porous and void surface. The SEM micrographs display agglomeration and the formation of

inhomogeneous grains with non-uniform grain size distribution. In addition to smaller particles, some larger particles are also observed, and more agglomeration exists [42]. The micrographs indicate that some dark portions may be created by the released gases during the citrate combustion method. The agglomeration formation is attributed to the greater surface area of the developed particles and the force of attraction in magnetic ions [43].

3.3 Dielectric Analysis

The dielectric characteristics of *CCCF-soft ferrites* are analyzed by an LCR meter. The dielectric characteristics are associated with the synthesis procedure, stoichiometric calculations, cation distribution, oxygen parameter, and sintering temperature [44]. Dielectric constant (ε′) was identified by the formula as,

$$\acute{\boldsymbol{\varepsilon}} = \frac{CD}{\varepsilon^{\circ}A} \qquad (18)$$

Where, C is capacitance, A and d are the area and thickness of the pellet, and ε^{o} is the permittivity of free space [45]. Fig. 5 shows the dielectric constant is exponentially decreasing for x = 0.0, 0.2 – 0.5 soft ferrites. For x = 0.1 sample dielectric constant has a linear nature. Previously in the literature, the dielectric constant exhibited a constant behavior at a frequency of 100 kHz, as observed in the Co-Zr substituted M-type calcium hexagonal ferrites by Chetna C. Chauhan *et al.,* [43]. Furthermore, all samples displayed a constant behavior after a frequency of 1.0 MHz, attributed to the electron hopping between iron ions ($Fe^{3+}\leftrightarrow Fe^{2+}$) [32] for *CCCF-soft ferrites,* leading to polarization. The introduction of Cr^{3+} ions is accountable for the decrease in polarization. Soft ferrites consist of conductive grains forming the primary layer and a resistive layer of grain boundaries as the secondary layer. Surface polarization arises from localized charge

distribution when an external field is applied. The Koops theory explains both the dielectric constant and dielectric loss. According to this theory, at lower frequencies with fewer conductive grain boundaries involved, a greater energy input is necessary to facilitate electron transfer between Fe^{2+} and Fe^{3+} ions. This phenomenon results in a more pronounced dielectric loss. Conversely, in high-frequency regions where the grains are actively participating, the dielectric loss is diminished as a higher energy requirement is needed for electron transport [46]. Dielectric loss can be categorized into three types: conduction, dipole, and vibration losses. Conduction loss occurs when ions undergo movement over significant distances, resulting in the transfer of energy to the surrounding lattices in the form of heat. The steady nature of the dielectric constant in high-frequency regions indicates that the synthesized ferrites are favorite candidates for microwave devices [33]. Fig. 5 gives the decrease in dielectric loss (Tanδ) by increasing the frequency for *CCCF-soft ferrites* [47]. Such presented nature of Tanδ may be due to the decline in the conduction mechanism. Soft conducting grains are distinct from the low-energy conducting grains in soft ferrites. In low-frequency regions, the activation of conducting grains decreases due to high energy demands for the hopping mechanism and causing the increase in Tanδ in the low- frequency regions. The conducting grains are obtained with more potential in high-frequency regions and thus a small amount of energy is required for the hopping process [32]. In addition, Tanδ is showing an exponential decreasing trend after the 0.1 MHz frequency as given in Fig. 5. Furthermore, the lowest dielectric losses are demonstrated by the x = 0.1 sample. The entire information of electrical properties of spinel ferrites depending upon their impedance of electrodes, ionic distribution, ceramic texture, and grain and grain boundary contributions is known as impedance [48]. The tangent loss is associated with an increase in resistivity. In low frequency, with high resistivity, the dielectric loss is formulated which plays a major role [45]. This kind of

normal performance of soft ferrites is due to the lagging of hopping electrons existing between Fe^{3+} and Fe^{2+} ions at different lattice sites. Moreover, Fe^{2+} ions cause various forms of polarization with the increasing applied electric field. Due to the increase in frequency, such phenomena occur at high temperatures during sintering [12]. Fig. 5 shows the graph of real impedance with the increase of frequency for *CCCF-soft ferrites*. It can be observed that real impedance is showing the same behavior for all ferrites except the x = 0.1 specimen. In x = 0.1 impedance is exponentially decreasing and also has maximum impedance. Such nature of impedance is associated with the interaction between dopant and replaced ions [32]. The imaginary part of the impedance is demonstrated in Fig. 5. From Fig. 5 it can be observed that the imaginary part of the impedance is exponentially decreasing with the enhancement of Cr^{3+} concentration and the trend becomes linear after 0.1 MHz frequency. Such behavior explains the presence of a relaxation process in soft ferrites. The relaxation process occurs due to the presence of static species at lower concentrations and defects are void at higher concentrations [41]. AC conductivity means the ability of ferrites to conduct electric current and it is given by the following relation [49],

$$\partial ac = 2\Pi f tan\delta \qquad (19)$$

From Fig. 5, it is clear that the AC conductivity, determined by the above equation, has a maximum value at x = 0.3 at room temperature. It was also noted from Fig. 5 that by increasing the frequency, AC conductivity also increased, but at low frequencies, it was found to be independent. This type of behavior in ferrites is reported in Maxwell-Wagner and Koop's phenomenological theories [50].

The grain boundaries (grain boundaries layers) which are more active and provide hindrance in the movement of charges, less hoping of Fe^{2+} and Fe^{3+} cations, and low ac conductivity were observed at low frequency. At higher frequencies, grains are more active which promotes hopping

electrons between Fe^{2+} and Fe^{3+} cations that take part in the formation of more charge barriers. Due to this behavior, hindrance to the mobility of charges was reduced, and AC conductivity increased, which is in agreement with the literature [12]. Fig. 6 shows the Cole-Cole plot between $M^{'}$ (real part of the electric modulus) and $M^{''}$ (imaginary part of the electric modulus) for *CCCF-soft ferrites*. The Cole-Cole graph explains the relaxation phenomena for conductive parts of grains to resistive interfaces in ferrites. Fig. 6 shows a significant bend for all *CCCF-soft ferrites* except x = 0.1 sample. This bend confirms the resistive outcomes of interfaces are leading to the conduction effects of grains. These electric modulus spectra also confirm the non-Debye relaxation due to conduction [41].

3.4 Molecular vibrational analysis

The modes of vibrations of *CCCF-soft ferrites* with 200 - 800 cm^{-1} intensity of Raman spectra are used along with Lorentz fit spectra as given in Fig. 7(A-F). In the IR region, as expected by the Brillouin zone group theory, the spinel structure of *CCCF-soft ferrites* have five active Raman modes: A_{1g}, E_g and $3T_{2g}$ ($T_{2g}(1)$, $T_{2g}(2)$, $T_{2g}(3)$) at room temperature [51]. The one, two and three dimensions are represented by A, E and T, respectively while the center of inversion symmetry is denoted by g [40]. The observed active Raman modes in *CCCF-soft ferrites* are reported in Table 5. Raman modes established on the quasi-molecular categorization of spinel structure related to normal mode arrangements of tetrahedron ($Fe - O_4$) as; The $T_{2g}(1)$ mode is related to translational movement of entire tetrahedron ($Fe - O_4$) ions [32] in the range of 291.7 - 325.3 cm^{-1}. The E_g mode of molecular vibration is related to the symmetric bending of oxygen at the octahedral site [40] and is appearing between 355.3 - 76.4 cm^{-1}. The $T_{2g}(2)$ modes are related to symmetric stretching

vibrations of (Fe – O) bonds at the tetrahedral site [32] and are lying in the range of 459.6–462.0 cm^{-1}. $T_{2g}(3)$ modes are present at tetrahedral sites and are related to the asymmetric bending of oxygen [40] in the range of 581.9–537.7 cm^{-1}. The A_{1g} modes of vibrations are present at (Fe – O) tetrahedral site and are related to the symmetric stretching of oxygen atoms [32] in the ranges of 712.1–666.5 cm^{-1}. Furthermore, in Fig. 7, some extra modes are appearing in *CCCF-soft ferrites*. Such modes are due to the presence of few impurities present in prepared samples.

3.5 DC electrical resistivity measurement

By using a two-probe instrument with Keithley I-V electrometer model 2401, current-voltage (I-V) graphs were recorded within the 313 - 623 K range of temperature for *CCCF-soft ferrites*. Fig. 7(A) demonstrates the distinctions in DC resistivity of prepared ferrites vs. temperature. The values of resistivity are found by the equation as [52],

$$\rho = \frac{RA}{L} \qquad (20)$$

Where, ρ represents the resistivity of prepared materials, A and L represent the surface area and thickness of all pellets, respectively [53]. The value of resistance was calculated by using the R=1/slope formula. Fig. 8(A) shows that DC resistivity is decreasing with the growth of Cr^{3+} contents. Hence, this fact is advantageous; ions of Cr^{3+} replace Fe^{3+} ions at B sites and cause a decline in DC electrical resistivity. The resistivity of prepared samples firstly increases with the enhancement of temperature from room temperature to 363 K and then starts decreasing continuously as the temperature rises. The value from where the temperature starts decreasing represents the Curie temperature (T_c). The T_c for x = 0.1 to x = 0.5 were observed at 383 K, 363 K, 403 K, 423 K, 423 K and 403 K, respectively. The corresponding results of DC resistivities at

given T_c for x = 0.0 to x = 0.5 nanoferrites are 6.8 x 10^8 ohm-cm, 5.1 x 10^8 Ohm-cm, 1.9 x 10^8 Ohm-cm, 8.2 x 10^7 Ohm-cm, 4.7 x 10^7 Ohm-cm, and 6.9 x 10^7 Ohm-cm, respectively. In literature, the highest DC resistivity (77.9 x 10^6 Ohm-cm) in pure and chromium substituted cobalt nanoferrites was observed by Raghasudha *et al.* at 300 K temperature [12]. The decrease in DC resistivity is ascribed to an escalation in the drift mobility of charge carriers [32]. Furthermore, maximum DC resistivity is expressed by the x = 0.0 sample confirming that the sample is more suitable for transformers to eliminate the eddy current harms. Also, the decreasing behavior of DC resistivity is due to the fact that Cr^{3+} has lower electrical conductivities (7.7 x 10^6 $(Ohm.m)^{-1}$) than Fe^{3+} (9.9 x 10^6 $(Ohm.m)^{-1}$). The region before Curie temperature (T_c) represents a ferromagnetic nature and the region after Curie temperature represents a paramagnetic nature as given in Fig. 8(B). Also, Fig. 8(B) demonstrates the relation between the log of DC resistivity and the inverse of temperature. The results revealed the semiconductor behavior of synthesized nanoferrites due to the rise in drift mobility (μ_d) of charge carriers with rising temperature [33]. Also, the Curie temperature (T_c) creates magnetic disorder in nano-ferrites and changes the behavior of nanoferrites from ferromagnetism to para-magnetism during conducting [34]. Fig. 8(C-F) shows the graphs for DC resistivities at different regions of temperature and activation energy for *CCCF-soft ferrites*. Fig. 8(C) shows the resistivity increases with the increase of temperature for x = 0.0 and 0.1 and maximum resistivity is shown by x = 0.1 in low-temperature regions. Fig. 8(D) shows the ranges of the medium temperature regions and shows the decrease in resistivity with the increase in temperature. Fig. 8(E) shows the graph of resistivities in high-temperature regions which is similar to the medium-temperature regions. The Arrhenius plot for activation energies [54] of *CCCF-soft ferrites* is illustrated in Fig. 8(F). The values of activation energies for composed soft ferrites are 0.9 eV (x = 0.0), 0.6 eV (x = 0.1), 0.9 eV (x = 0.2), 0.8 eV (x = 0.3), 0.8

eV (x = 0.4) and 0.9 eV (x = 0.5). Fig. 8(G) demonstrates the calculated values of the percentage temperature coefficient of resistance (TCR%) by the use of temperature-dependent DC electrical resistivity for all *CCCF-soft ferrites*. The composed ferrites presented the temperature-dependent TCR peaks at 453K temperature. The peak location of temperature against TCR% curves for the composed ferrites are as follows: -1.2 K^{-1} (x = 0.0), -1.3 K^{-1} (x = 0.1), -0.5 K^{-1} (x = 0.2), -0.2 K^{-1} (x = 0.3), -0.2 K^{-1} (x = 0.4) and -0.5 K^{-1} (x = 0.5). The TCR% results are associated with the sintering duration and temperature [55]. The determined ranges of TCR% values suggested that *CCCF-soft ferrites* are suitable for bolometric applications [56].

3.6 Magnetic properties

The hysteresis loop for *CCCF-soft ferrites* at room temperature is presented in Fig. 9. From Fig. 9, it can be observed that all composed ferrites exhibit a similar magnetic nature. Hysteresis loop can be used to measure different parameters such as saturation magnetization (M_s), remanence magnetization (M_r), and coercivity (H_c) [3, 57] as reported in Table 6. The saturation magnetization has a variable trend with the increase of Cr^{3+} concentrations. The anomalous factor is responsible for such variable behavior [58]. Also, the variable trend of M_s is associated with the presence of some secondary phases [32]. The coercivity (H_c) has also shown variable behavior with increments of Cr^{3+} ions as given in Table 6. The highest saturation magnetization and coercivity are illustrated by x = 0.4 (61.9 emu/g) and x = 0.3 (1242.6 Oe), respectively. Previously, the highest saturation magnetization (36.9 emu/g) and coercivity (34.0 Oe) in the Mg–Zn–Cr ferrites was reported by

Mehmat Kuru *et al.,* [26]. The magnetic characteristics of soft ferrites typically depend on factors such as grain size, synthesis technique, and the distribution of cations.

Furthermore, the coercivity (H_c) of soft ferrites depends upon magneto-crystalline anisotropy, the interaction between the particle's micro-strain, temperature, and size of particles [26]. The behavior of H_c can be described by the Stoner-Wohlfarth principle [59]. The variations in M_s could be advocated by two factors i) crystallite size and ii) cations distributions [60].The decrease in crystallite leads to a decrease in saturation magnetization. While, the increase in M_s is attributed to an increase in magnetic behavior at the octahedral site due to cations distribution [26, 61] and this fact can be observed in Table 4. Due to the significant influence of cation placement on anisotropy, measuring coercivity serves as a precise method for tracking cation migrations when Cr ions are introduced. Moreover, the alteration in the unit cell structure, the arrangement of the octahedral Cr ions, and the particle's shape anisotropy collectively contribute to the development of increased coercivities in *CCCF-soft ferrites* [62]. M_s declines as the weak magnetic Cr^{3+} (3.8 μB) ions replace the stronger magnetic Fe^{3+} (5.9 μB) ions at B-site [26]. The remanence magnetization (M_r) has a similar trend to M_s as given in Table 6. The influence of cation distribution on the magnetization of *CCCF-soft ferrites* can be explained through Neel's two-sublattice model. In this model, the magnetic orientation of cations residing on the A and B sublattices is such that they align in an antiparallel manner, and their spins exhibit a collinear arrangement. Consequently, the saturation magnetization of spinel ferrite is contingent upon the distribution of cations between the A and B sites. The overall magnetization per formula unit can be expressed as $M = M_B - M_A$, with M_B and M_A representing the magnetization values of the B and A sublattices, correspondingly [63]. The magnetic moments for the A-site lie in the ranges of 0.04676 μB, 0.06243 μB, 0.06612 μB, 0.03867 μB, 0.1031 μB, and 0.06946 μB. While, the

magnetic moments for the B-site lie in the range of 0.1094 μB, 0.1455 μB, 0.1536 μB, 0.0895 μB, 0.2380 μB, and 0.1597 μB. The difference in magnetizations lies in the range of 0.06263 μB, 0.08312 μB, 0.08751 μB, 0.05087 μB, 0.1348 μB, and 0.09027 μB. The Cr^{3+} has an inverse spinel structure and resides on the B-site and Fe^{3+} resides on both A and B sites. So, the net magnetic moments of Fe^{3+} ions (5.9 μB) cancel and the net magnetic moment is due to the Cr^{3+} ions (3 μB). By increasing the Cr^{3+} concentration, the net magnetic moment also increases. Therefore, it can be observed that the net magnetic moment exhibits an increasing behavior, which is in agreement with the cation distributions on the tetrahedral site, as illustrated in Table 3.

The squareness (S.Q) or M_r/M_s ratio [58] describes the inter-grain interchange in soft ferrites by approaching the three ways i) S.Q<1/2 i.e., nanoferrites interrelates magneto-statically, ii) S.Q = 1/2 i.e., the nanoferrites are distributed randomly and have no interaction ability, iii) ½<S.Q<1 i.e., the presence of interchange coupling is carried on [26]. In *CCCF-soft ferrites*, since the S.Q ratio is less than ½ the nanoferrites have magneto-statically interacting ability as tabulated in Table 6. The Bohr's magneton (μB) for magnetic moment per formula [4] was determined in the range of 0.2 - 0.3 μB for x = 0.0 - 0.5, respectively. From Table 6 the variable behavior is demonstrated by "n_B" due to the substitution of low magnetic Cr^{3+} ions with stronger magnetic Fe^{3+} ions which also caused the same behavior for M_s. The determined results for anisotropy constant (K) [64] and initial permeability (μ_i) [40] are also reported in Table 6. The anisotropy constant firstly increases from 28122.4 erg/cm^3 to 43761.8 erg/cm^3 for x = 0.0 to x = 0.1 and then drops to 27168.5 erg/cm^3 (x = 0.2) then again increases from 29977.4 erg/cm^3 to 50275.8 erg/cm^3 for x = 0.3 to x = 0.4 and then again decreases to 41820.1 erg/cm^3 (x = 0.5). The higher anisotropy constant indicates the restricted free and easy domain wall motion of ions [65]. The initial permeability is associated with the molecular weight and M_s [40]. Hence, μ_i behaves similarly to saturation magnetization.

This behavior can also be attributed to the decline in crystallite size with the addition of Cr^{3+}The Yafet and Kittel (Y–K) angle or spin canting angle ($\alpha_{y\text{-}k}$) [32] are also given in Table 6. The increasing nature shown by *CCCF-soft ferrites* is confirmed by the increasing nature of tetrahedral ionic radii [26]. The microwave frequency (ω_m) [57] values are reported in Table 6. The obtained values of "ω_m" confirm the applications of *CCCF-soft ferrites* in longitudinal media and microwave absorbance [32].

Conclusion

Cr^{3+} was introduced into Ca-Co soft ferrites through the sol-gel auto-combustion process. X-ray diffraction (XRD) analysis was utilized to determine the material's crystalline structure, phase identification, and unit cell dimensions, with a crystallite size below 50 nm, indicating their potential use in recording media. Scanning electron microscopy (SEM) micrographs depicted the surface morphology and nanoparticle agglomeration, while an increase in Cr^{3+} concentration led to a reduction in dielectric constant, loss, and impedance. The Dielectric parameters exhibited a continuous trend at higher frequencies, and Raman spectroscopy revealed vibrational modes in both tetrahedral and octahedral sites. DC electrical resistivity decreased within a range from 6.8 x 10^8 ohm·cm to 6.9 x 10^7 ohm·cm at Curie temperatures, and the TCR (%) values suggested their suitability for bolometric applications. The highest and lowest saturation magnetization and coercivity values occurred at (x = 0.4 and 0.3), and (x = 0.3 and 0.2), respectively. The dielectric constant and microwave frequency ranges affirmed the material's suitability for longitudinal recording media and microwave devices.

Funds for Fellowship

Muhammad Imran Arshad would like to thank HEC Pakistan for giving opportunity of Postdoc under post doc batch 3 (Ref: 3-1/PDFP/HEC/2022(B-3)/2320/02). He also extends his appreciation to University College London, London, U.K., for hosting this fellowship.

Acknowledgments

The authors extend their appreciation to the Deanship of Scientific Research at King Khalid University, Abha, Saudi Arabia, for funding this work through the Research Groups Program, under grant no. R.G.P.2-2/475/44.

References

[1] S. B. Somvanshi, P. B. Kharat, T. S. Saraf, S. B. Somwanshi, S. B. Shejul, K. M. Jadhav, Multifunctional nano-magnetic particles assisted viral RNA-extraction protocol for potential detection of COVID-19, Materials Research Innovations, 25 (2021) 169-174.

[2] M. Hasan, S. Ali, M. Khan, M. Rizwan, M. Zulqarnain, A. Hussain, Structural, optical, electrical and magnetic tuning based on Zn substitution at a site in yttrium doped spinel ferrites, Materials Chemistry and Physics, (2023) 127538.

[3] M. Hasan, S. Ali, M. Rizwan, M. Khan, H.N. Ullah, M.I. Irfan, Structural, optical, electrical and magnetic properties of Cu0. 2Zn0. 2Ni0. 6-xMgxFe2O4 (x= 0.00, 0.15, 0.30, 0.45, 0.60) soft ferrites, Journal of Alloys and Compounds, 956 (2023) 170392.

[4] M. Khan, M. Waqas, M. Naeem, M. Hasan, M. Iqbal, A. Mahmood, S.M. Ramay, W. Al-Masry, S.A. Abubshait, H.A. Abubshait, Magnetic behavior of Ga doped yttrium iron garnet ferrite thin films deposited by sol-gel technique, Ceramics International, 46 (2020) 27318-27325.

[5] Y. Luo, J. Liu, H. Yang, H. Liu, G. Zeng, B. Huang, Enhanced Circular Dichroism by F-Type Chiral Metal Nanostructures, in: Photonics, MDPI, 2023, pp. 1028.

[6] J. Wang, Y. Zhang, G. Liu, T. Zhang, C. Zhang, Y. Zhang, Y. Feng, Q. Chi, Improvements in the Magnesium Ion Transport Properties of Graphene/CNT-Wrapped TiO2-B Nanoflowers by Nickel Doping, Small, (2023) 2304969.

[7] Y. Zhao, Y. Sun, H. Hou, Core-shell structure nanoprecipitates in Fe-xCu-3.0 Mn-1.5 Ni-1.5 Al alloys: A phase field study, Progress in Natural Science: Materials International, 32 (2022) 358-368.

[8] L. Klein, M. Aparicio, A. Jitianu, Handbook of sol-gel science and technology: Processing, characterization and applications, Springer Nature, 2018.

[9] M. Azim, M. Chaudhry, N. Amin, M. Arshad, M. Islam, S. Nosheen, M. Ahmad, H. Anwar, M. Waseem, G. Mustafa, Structural and optical properties of cr-substituted co-ferrite synthesis by coprecipitation method, Digest J Nanomaterial Bio structures, 11 (2016) 953-962.

[10] S. Gurav, S.E. Shirsath, R. Kadam, D. Mane, Low temperature synthesis of Li0. 5ZrxCoxFe2. 5− 2xO4 powder and their characterizations, Powder technology, 235 (2013) 485-492.

[11] S. More, R. Kadam, A. Kadam, A. Shite, D. Mane, K. Jadhav, Cation distribution in nanocrystalline Al3+ and Cr3+ co-substituted CoFe2O4, Journal of alloys and compounds, 502 (2010) 477-479.

[12] M. Raghasudha, D. Ravinder, P. Veerasomaiah, Influence of Cr 3+ ion on the dielectric properties of nano crystalline Mg-ferrites synthesized by citrate-gel method, (2013).

[13] M. Raghasudha, D. Ravinder, P. Veerasomaiah, Investigation of superparamagnetism in pure and chromium substituted cobalt nanoferrite, Journal of Magnetism and Magnetic Materials, 420 (2016) 45-50.

[14] X. Wang, X. Li, H. Xie, T. Fan, L. Zhang, K. Li, Y. Cao, X. Yang, B. Liu, P. Bai, Effects of Al and La elements on mechanical properties of CoNiFe0. 6Cr0. 6 high-entropy alloys: a first-principles study, Journal of Materials Research and Technology, 23 (2023) 1130-1140.

[15] M. Zahid, H.M. Khan, I. Sadiq, K. Ali, M. Mirza, M. Islam, S.A. Buzdar, Enhanced structural and dielectric properties of calcium and chromium based M-type hexagonal ferrites, Journal of Materials Science: Materials in Electronics, 32 (2021) 9183-9193.

[16] J. Zhao, J. Gao, W. Li, Y. Qian, X. Shen, X. Wang, X. Shen, Z. Hu, C. Dong, Q. Huang, A combinatory ferroelectric compound bridging simple ABO3 and A-site-ordered quadruple perovskite, Nature communications, 12 (2021) 747.

[17] S. Gowreesan, A.R. Kumar, Synthesis, structural, dielectric and magnetic properties of spinel structure of Ca2+ substitute in Cobalt ferrites (Co1− xCaxFe2O4), Chinese journal of physics, 56 (2018) 1262-1272.

[18] R. Kumar, M. Kar, Correlation between lattice strain and magnetic behavior in non-magnetic Ca substituted nano-crystalline cobalt ferrite, Ceramics International, 42 (2016) 6640-6647.

[19] S. Sarmah, D. Maji, S. Ravi, T. Bora, Effect of Cr3+ substitution on the magnetic and dielectric properties of cobalt ferrites, Journal of Alloys and Compounds, 960 (2023) 170589.

[20] M. Hasan, M. Khan, M. Amami, S. Ezzine, Exploring the structural, morphological, optical, electrical, dielectric and magnetic properties of Co2+ doped Cd0. 4Zn0. 6-xFe1. 9Sm0. 1O4 soft ferrites prepared by green synthesis method, Ceramics International, 50 (2024) 3129-3138.

[21] M.I. Khan, M. Touheed, M. Sajjad-ul-Hasan, M. Siddique, S.A. Rouf, T. Ahmad, M. Fatima, M. Iqbal, M.M. Almoneef, N. Alwadai, Hydrothermal synthesis, characterization and photocatalytic activity of Mg doped MoS2, Zeitschrift für Physikalische Chemie, 236 (2022) 155-168.

[22] M.N. Ashiq, M.F. Ehsan, M.J. Iqbal, I.H. Gul, Synthesis, structural and electrical characterization of Sb3+ substituted spinel nickel ferrite (NiSbxFe2− xO4) nanoparticles by reverse micelle technique, Journal of Alloys and Compounds, 509 (2011) 5119-5126.

[23] A.B. Bhosale, S.B. Somvanshi, V. Murumkar, K. Jadhav, Influential incorporation of RE metal ion (Dy3+) in yttrium iron garnet (YIG) nanoparticles: Magnetic, electrical and dielectric behaviour, Ceramics International, 46 (2020) 15372-15378.

[24] S. Che, J. Wang, Q. Chen, Soft magnetic nanoparticles of BaFe12O19 fabricated under mild conditions, Journal of physics: condensed matter, 15 (2003) L335.

[25] M. Hasan, M. Khan, S. Kanwal, M. Irfan, T.I. Al-Muhimeed, S. Mumtaz, Structural, optical and electrical impacts of Ni 2+ on Mg 1-x Fe 1.9 Sm 0.1 O 4 (x= 0.0, 0.2, 0.4 and 0.6) spinel ferrites, Digest Journal of Nanomaterials & Biostructures (DJNB), 17 (2022).

[26] M. Kuru, T.Ş. Kuru, E. Karaca, S. Bağcı, Dielectric, magnetic and humidity properties of Mg–Zn–Cr ferrites, Journal of Alloys and Compounds, 836 (2020) 155318.

[27] S.B. Somvanshi, S.A. Jadhav, M.V. Khedkar, P.B. Kharat, S. More, K. Jadhav, Structural, thermal, spectral, optical and surface analysis of rare earth metal ion (Gd3+) doped mixed Zn–Mg nano-spinel ferrites, Ceramics International, 46 (2020) 13170-13179.

[28] M. Hasan, M. Arshad, A. Ali, K. Mahmood, N. Amin, S. Ali, M. Khan, G. Mustafa, M. Khan, M. Saleem, Mg and La co-doped ZnNi spinel ferrites for low resistive applications, Materials Research Express, 6 (2018) 016302.

[29] V. Bharati, S.B. Somvanshi, A.V. Humbe, V. Murumkar, V. Sondur, K. Jadhav, Influence of trivalent Al–Cr co-substitution on the structural, morphological and Mössbauer properties of nickel ferrite nanoparticles, Journal of Alloys and Compounds, 821 (2020) 153501.

[30] W.A. Farooq, M. Sajjad Ul Hasan, M.I. Khan, A.R. Ashraf, M. Abdul Qayyum, N. Yaqub, M.A. Almutairi, M. Atif, A. Hanif, Structural, Optical and Electrical Properties of Cu0. 6CoxZn0. 4− xFe2O4 (x= 0.0, 0.1, 0.2, 0.3, 0.4) Soft Ferrites, Molecules, 26 (2021) 1399.

[31] M.A.U. Nabi, M. Moin, M. Hasan, M. Arshad, A. Bibi, N. Amin, K. Mahmood, S. Ali, Study of electrical transport properties of cadmium-doped Zn–Mn soft ferrites by co-precipitation method, Journal of Superconductivity and Novel Magnetism, 34 (2021) 1813-1822.

[32] M. Akhtar, M. Hasan, N. Amin, N. Morley, M.I. Arshad, Tuning structural, electrical, dielectric and magnetic properties of Mg–Cu–Co ferrites via dysprosium (Dy3+) doping, Journal of Rare Earths, (2023).

[33] A. Mujtaba, M. Khan, M. Hasan, S. Ali, W. Shahid, M. Fatima, H.S. Abd-Rabboh, N. Alwadai, Tailoring the structural, optical, photoluminescence, dielectric and electrical properties of Zn0. 6Ni0. 2Mg0. 2Fe2-xLaxO4 (x= 0.00, 0.0125, 0.0250, 0.0375), Journal of Materials Research and Technology, (2023).

[34] N. Amin, M.S.U. Hasan, Z. Majeed, Z. Latif, M.A. un Nabi, K. Mahmood, A. Ali, K. Mehmood, M. Fatima, M. Akhtar, Structural, electrical, optical and dielectric properties of yttrium substituted cadmium ferrites prepared by Co-Precipitation method, Ceramics International, 46 (2020) 20798-20809.

[35] A. Birajdar, S.E. Shirsath, R. Kadam, S. Patange, D. Mane, A. Shitre, Frequency and temperature dependent electrical properties of Ni0. 7Zn0. 3CrxFe2− xO4 (0≤ x≤ 0.5), Ceramics International, 38 (2012) 2963-2970.

[36] M. Hashim, S. Meena, R. Kotnala, S.E. Shirsath, P. Bhatt, S. Kumar, E. Şentürk, R. Kumar, N. Gupta, Exploring the structural, Mössbauer and dielectric properties of Co2+ incorporated Mg0.

5Zn0. 5− xCoxFe2O4 nanocrystalline ferrite, Journal of magnetism and magnetic materials, 360 (2014) 21-33.

[37] T. Vigneswari, P. Raji, Structural and magnetic properties of calcium doped nickel ferrite nanoparticles by co-precipitation method, Journal of Molecular Structure, 1127 (2017) 515-521.

[38] Y. Li, Y. Ma, S. Ye, G. Hu, Q. Zhang, Site-related near-infrared luminescence in MAl12O19 (M= Ca, Sr, Ba): Fe3+ phosphors, Materials Research Bulletin, 51 (2014) 1-5.

[39] M. Saqib, S. Ali, M. Zulqarnain, M.U. Qadri, M. Riaz, M. Hasan, M. Khan, M. Tahir, M. Arshad, H. Rani, Temperature-dependent variations in structural, magnetic, and optical behavior of doped ferrites nanoparticles, Journal of Superconductivity and Novel Magnetism, 34 (2021) 609-616.

[40] M.I. Arshad, M. Hasan, A.U. Rehman, M. Akhtar, N. Amin, K. Mahmood, A. Ali, T. Trakoolwilaiwan, N.T.K. Thanh, Structural, optical, electrical, dielectric, molecular vibrational and magnetic properties of La3+ doped Mg–Cd–Cu ferrites prepared by Co-precipitation technique, Ceramics International, 48 (2022) 14246-14260.

[41] M. Zulqarnain, S. Ali, U. Hira, J. Feng, M. Khan, M. Rizwan, K. Javed, G. Farid, M. Hasan, Superparamagnetic contributions, optical band gap tuning and dominant interfacial resistive mechanisms in ferrites nanostructures, Journal of Alloys and Compounds, 894 (2022) 162431.

[42] S.Y. Mulushoa, N. Murali, M.T. Wegayehu, S. Margarette, K. Samatha, Influence of Cu-Cr substitution on structural, morphological, electrical and magnetic properties of magnesium ferrite, Results in physics, 8 (2018) 772-779.

[43] C.C. Chauhan, A.R. Kagdi, R.B. Jotania, A. Upadhyay, C.S. Sandhu, S.E. Shirsath, S.S. Meena, Structural, magnetic and dielectric properties of Co-Zr substituted M-type calcium

hexagonal ferrite nanoparticles in the presence of α-Fe2O3 phase, Ceramics International, 44 (2018) 17812-17823.

[44] M.Y. Lodhi, M.A. Khan, M.N. Akhtar, M.F. Warsi, A. Mahmood, S.M. Ramay, Role of Nd-Ni on structural, spectral and dielectric properties of strontium-barium based nano-sized X-type ferrites, Ceramics International, 44 (2018) 2968-2975.

[45] R. Magisetty, A.B. Raj, S. Datar, A. Shukla, B. Kandasubramanian, Nanocomposite engineered carbon fabric-mat as a passive metamaterial for stealth application, Journal of Alloys and Compounds, 848 (2020) 155771.

[46] Z. Wu, B. Lin, J. Fan, J. Zhao, Q. Zhang, L. Li, Effect of dielectric relaxation of epoxy resin on dielectric loss of medium-frequency transformer, IEEE Transactions on Dielectrics and Electrical Insulation, 29 (2022) 1651-1658.

[47] R. Weast, Handbook of Chemistry and Physics, 64th E d itio n, CRC P ress, In c., Boca Raton, F lorida, (1984).

[48] A. ur Rahman, M. Rafiq, K. Maaz, S. Karim, K. Hayat, M. Hasan, Correlation between magnetic and electrical properties of Co 0.6 Sn 0.4 Fe 2 O 4 nanoparticles, Journal of nanoparticle research, 16 (2014) 1-8.

[49] S. Ikram, M.I. Arshad, K. Mahmood, A. Ali, N. Amin, N. Ali, Structural, magnetic and dielectric study of La3+ substituted Cu0. 8Cd0. 2Fe2O4 ferrite nanoparticles synthesized by the co-precipitation method, Journal of Alloys and Compounds, 769 (2018) 1019-1025.

[50] N. Yasmin, M. Zahid, H.M. Khan, M. Hashim, M.U. Islam, S. Yasmin, M. Altaf, B. Nazar, M. Safdar, M. Mirza, Structural and dielectric properties of Gd-Zn substituted Ca0.5Ba0.5Fe12O19 M-type hexa-ferrites synthesized via auto-combustion method, Journal of Alloys and Compounds, 774 (2019) 962-968.

[51] K.S.A. Kumar, R.N. Bhowmik, Micro-structural characterization and magnetic study of Ni1.5Fe1.5O4 ferrite synthesized through coprecipitation route at different pH values, Materials Chemistry and Physics, 146 (2014) 159-169.

[52] N. Amin, R. Bilal, G. Mustafa, A. Aslam, M. Hasan, K. Hussain, M. Tabassum, M. Fatima, Z. Khan, A. Naseem, IMPACTS OF SUBSTITUTING Ni 2 IONS ON STRUCTURAL AND ELECTRICAL PROPERTIES OF W-TYPE BARIUM BASED HEXAFERRITES, Digest Journal of Nanomaterials and Biostructures, 14 (2019) 501-507.

[53] M. Arshad, M. Hasan, A.U. Rehman, N. Amin, N.K. Thanh, N. Morley, M. Amami, F. Alresheedi, S. Ezzine, M. Gadhi, Mg-modified Zn-Co-Fe-La nano ferrites: A study of structural, morphological, vibrational, electro-optical, dielectric and magnetic evolution, Journal of Alloys and Compounds, 972 (2024) 172847.

[54] M. Fatima, M.S.U. Hasan, M. Akhtar, N. Morley, N. Amin, A.u. Rehman, M.I. Arshad, M. Amami, B. Yaqub, S. Ezzine, Comprehensive Improvement of Various Features of Cu–Cd Ferrites (Cu0. 5Cd0. 5Fe2–x Ce x O4) by Cerium (Ce3+) Ion Substitution, ACS omega, 8 (2023) 41169-41181.

[55] G. Abbas, A.U. Rehman, W. Gull, M. Afzaal, N. Amin, L. Ben Farhat, M. Amami, N.A. Morley, M. Akhtar, M.I. Arshad, Impact of Co2+ on the spectral, optoelectrical, and dielectric properties of Mg 0.25 Ni 0.25 Cu 0.5− x Co x Fe 1.97 La 0.03 O 4 ferrites prepared via sol–gel auto-combustion route, Journal of Sol-Gel Science and Technology, 101 (2022) 428-442.

[56] K. Mehmood, A.U. Rehman, N. Amin, N. Morley, M.I. Arshad, Graphene nanoplatelets/Ni-Co-Nd spinel ferrite composites with improving dielectric properties, Journal of Alloys and Compounds, 930 (2023) 167335.

[57] A.S. Gaikwad, S.E. Shirsath, S.R. Wadgane, R. Kadam, J. Shah, R. Kotnala, A. Kadam, Magneto-electric coupling and improved dielectric constant of BaTiO3 and Fe-rich (Co0. 7Fe2. 3O4) ferrite nano-composites, Journal of Magnetism and Magnetic Materials, 465 (2018) 508-514.

[58] R. Kadam, S.T. Alone, A.S. Gaikwad, A. Birajdar, S.E. Shirsath, Al3+ ions dependent structural and magnetic properties of Co–Ni nano-alloys, Journal of Nanoscience and Nanotechnology, 14 (2014) 4101-4107.

[59] Q. Zeng, I. Baker, V. McCreary, Z. Yan, Soft ferromagnetism in nanostructured mechanical alloying FeCo-based powders, Journal of Magnetism and Magnetic Materials, 318 (2007) 28-38.

[60] C. Caizer, M. Stefanescu, Magnetic characterization of nanocrystalline Ni–Zn ferrite powder prepared by the glyoxylate precursor method, Journal of Physics D: Applied Physics, 35 (2002) 3035.

[61] K. Bamzai, G. Kour, B. Kaur, S. Kulkarni, Effect of cation distribution on structural and magnetic properties of Dy substituted magnesium ferrite, Journal of magnetism and magnetic materials, 327 (2013) 159-166.

[62] S.E. Shirsath, R. Kadam, M. Mane, A. Ghasemi, Y. Yasukawa, X. Liu, A. Morisako, Permeability and magnetic interactions in Co2+ substituted Li0. 5Fe2. 5O4 alloys, Journal of alloys and compounds, 575 (2013) 145-151.

[63] S. Hunpratub, S. Phokha, P. Kidkhunthod, N. Chanlek, P. Chindaprasirt, The effect of cation distribution on the magnetic properties of CoFe2O4 nanoparticles, Results in Physics, 24 (2021) 104112.

[64] G. Todkar, R. Kunale, R. Kamble, K.M. Batoo, M. Ijaz, A. Imran, M. Hadi, E. Raslan, S.E. Shirsath, R. Kadam, Ce–Dy substituted barium hexaferrite nanoparticles with large coercivity for

permanent magnet and microwave absorber application, Journal of Physics D: Applied Physics, 54 (2021) 294001.

[65] S. Haralkar, R. Kadam, S. More, S.E. Shirsath, M. Mane, S. Patil, D. Mane, Substitutional effect of Cr3+ ions on the properties of Mg–Zn ferrite nanoparticles, Physica B: Condensed Matter, 407 (2012) 4338-4346.

Table 1: Cr^{3+} concentration (x), crystalline size (D), interplanar spacing (d), R-factor(R_{wp}, R_{exp}), goodness of fit (χ^2), lattice parameter (a), the experimental lattice constant (a_{exp}), dislocation line density (δ), unit cell volume (V), and densities (X-ray and bulk) for *CCCF-soft ferrites*

x	D (nm) ±0.1	d (Å)	a_{exp} (Å) ±0.0003	R_{wp}	R_{exp}	χ^2	a (Å)	δ (nm^{-2})	V $(Å)^3$	ρ_X (g/cm^3)	ρ_b (g/cm^3)
0.0	16.4	2.5	8.3	9.6	6.3	1.5	8.3	0.003	590.3	5.0	3.8
0.1	16.0	2.5	8.3	8.6	4.0	2.1	8.3	0.003	582.6	5.1	3.7
0.2	14.5	2.5	8.3	7.9	3.2	2.4	8.3	0.004	578.1	5.1	3.7
0.3	14.1	2.5	8.3	7.8	2.9	2.6	8.3	0.005	575.2	5.1	3.7
0.4	13.7	2.5	8.3	10.4	6.0	1.7	8.3	0.005	572.3	5.1	3.7
0.5	13.5	2.5	8.2	9.7	3.9	2.5	8.3	0.005	571.2	5.1	3.7

Table 2: Molecular weight (M), hopping length H_A, and H_B, packing factor (p), strain (ε), specific surface area (S), and polaron radius (γ_p) for *CCCF-soft ferrites*

x	*M* (g/mol)	H_A (Å)	H_B (Å)	*P*	*E*	*S* (m^2/g)	γ_p (Å)
0.0	225.1	3.6	2.9	65.0	0.007	71.8	0.7
0.1	224.8	3.6	2.9	63.8	0.007	72.7	0.7
0.2	224.4	3.6	2.9	58.0	0.008	79.7	0.7
0.3	224.0	3.6	2.9	56.3	0.008	82.0	0.7
0.4	223.6	3.5	2.9	55.1	0.008	83.7	0.7
0.5	223.2	3.5	2.9	54.0	0.008	85.4	0.7

Table 3: Cation Distribution of *CCCF-soft ferrites*

Composition	Tetrahedral site (A-site)	Octahedral Site (B-site)
$Ca_{0.5}Co_{0.5}Fe_2O_4$	$Ca^{2+}_{0.5} + Co^{2+}_{0.1} + Fe^{3+}_{0.4}$	$Co^{2+}_{0.4} + Fe^{3+}_{1.6}$
$Ca_{0.5}Co_{0.5}Cr_{0.1}Fe_{1.9}O_4$	$Ca^{2+}_{0.5} + Co^{2+}_{0.1} + Fe^{3+}_{0.4}$	$Co^{2+}_{0.4} + Cr^{3+}_{0.1} + Fe^{3+}_{1.5}$
$Ca_{0.5}Co_{0.5}Cr_{0.2}Fe_{1.8}O_4$	$Ca^{2+}_{0.5} + Co^{2+}_{0.1} + Fe^{3+}_{0.4}$	$Co^{2+}_{0.4} + Cr^{3+}_{0.2} + Fe^{3+}_{1.4}$
$Ca_{0.5}Co_{0.5}Cr_{0.3}Fe_{1.7}O_4$	$Ca^{2+}_{0.5} + Co^{2+}_{0.1} + Fe^{3+}_{0.4}$	$Co^{2+}_{0.4} + Cr^{3+}_{0.3} + Fe^{3+}_{1.3}$
$Ca_{0.5}Co_{0.5}Cr_{0.4}Fe_{1.6}O_4$	$Ca^{2+}_{0.5} + Co^{2+}_{0.1} + Fe^{3+}_{0.4}$	$Co^{2+}_{0.4} + Cr^{3+}_{0.4} + Fe^{3+}_{1.2}$
$Ca_{0.5}Co_{0.5}Cr_{0.5}Fe_{1.5}O_4$	$Ca^{2+}_{0.5} + Co^{2+}_{0.1} + Fe^{3+}_{0.4}$	$Co^{2+}_{0.4} + Cr^{3+}_{0.5} + Fe^{3+}_{1.1}$

Table 4: Theoretical structural parameters for *CCCF-soft ferrites*

x	r_A (Å)	r_B (Å)	a_{th} (Å)	U (Å)	T (Å)	R_A (Å)	R_B (Å)	R_x (Å)	R_x' (Å)	R_x'' (Å)
0.0	0.7	0.6	8.4	0.3	1.0	2.0	1.9	3.3	2.5	2.9
0.1	0.7	0.6	8.4	0.3	1.0	2.0	1.9	3.3	2.5	2.9
0.2	0.7	0.6	8.4	0.3	1.0	2.0	1.9	3.3	2.5	2.9
0.3	0.7	0.6	8.4	0.3	1.0	2.0	1.9	3.3	2.5	2.9
0.4	0.7	0.6	8.5	0.3	1.0	2.0	1.9	3.3	2.5	2.9
0.5	0.7	0.6	8.5	0.3	1.0	2.0	1.9	3.2	2.5	2.9

Table 5: Modes of Raman *CCCF-soft ferrites*

x	Raman Shift (cm^{-1})				
	$T_{2g}(1)$	E_g	$T_{2g}(2)$	$T_{2g}(3)$	A_{1g}
	A-site	B-site	A-site	A-site	A-site
0.0	291.7	355.3	459.6	581.9	679.7
0.1	306.9	344.9	468.5	578.6	675.2
0.2	316.0	340.7	450.8	511.6	712.1
0.3	321.5	344.5	464.5	563.1	686.4
0.4	327.4	358.6	454.1	584.2	666.5
0.5	325.3	376.4	462.0	537.7	679.3

Table 6: Different calculated magnetic parameters for *CCCF-soft ferrites*

x	H_C (Oe)	S.Q	M_r (emu/g)	M_s (emu/g)	n_B (μB)	K (erg/cm^3)	μ_i	α_{y-k} (Degree)	ω_m (GHz)
0.0	984.3	0.4	12.0	27.4	0.2	28122.4	0.4	29.5	6.0
0.1	1134.2	0.4	17.3	37.0	0.2	43761.8	0.5	38.2	8.1
0.2	660.8	0.6	25.4	39.4	0.3	27168.5	0.8	45.9	8.7
0.3	1242.6	0.4	10.2	23.1	0.1	29977.4	0.2	54.2	5.1
0.4	778.6	0.3	24.2	61.9	0.4	50275.8	1.0	57.0	13.6
0.5	961.7	0.4	17.2	41.7	0.3	41820.1	0.5	64.2	9.2

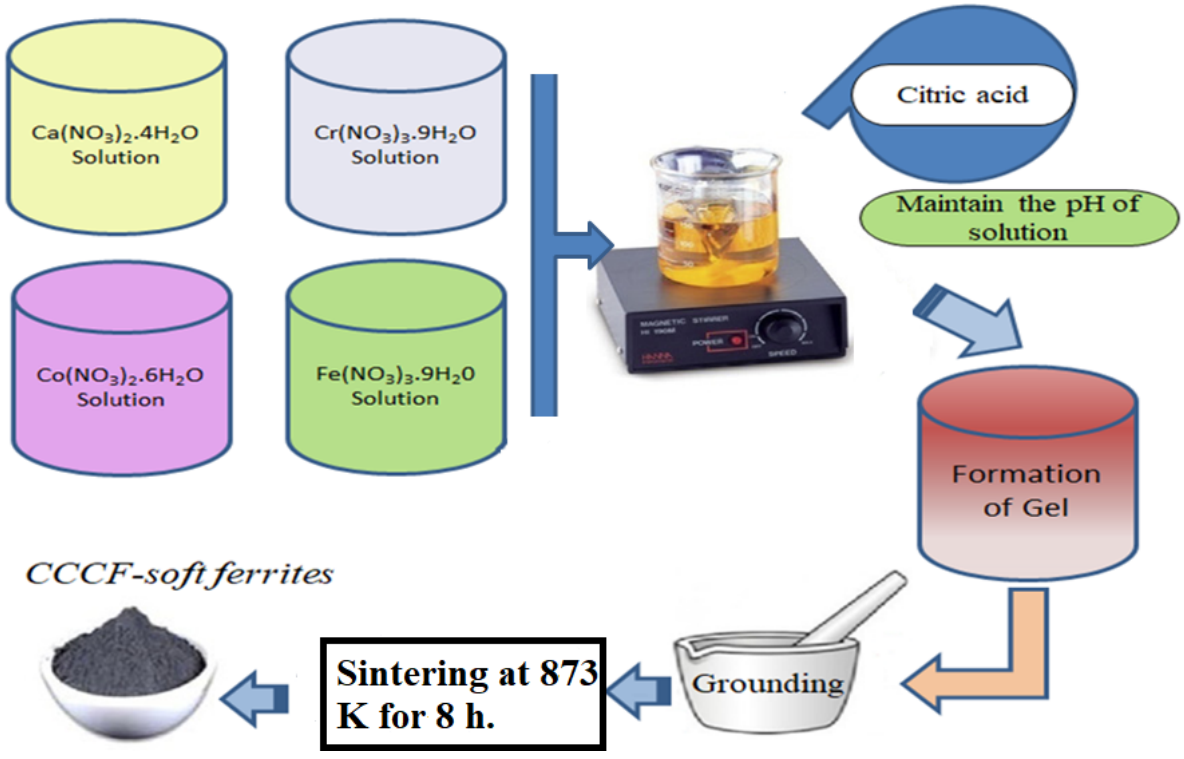

Fig 1: Schematic diagram of *CCCF-soft ferrites.*

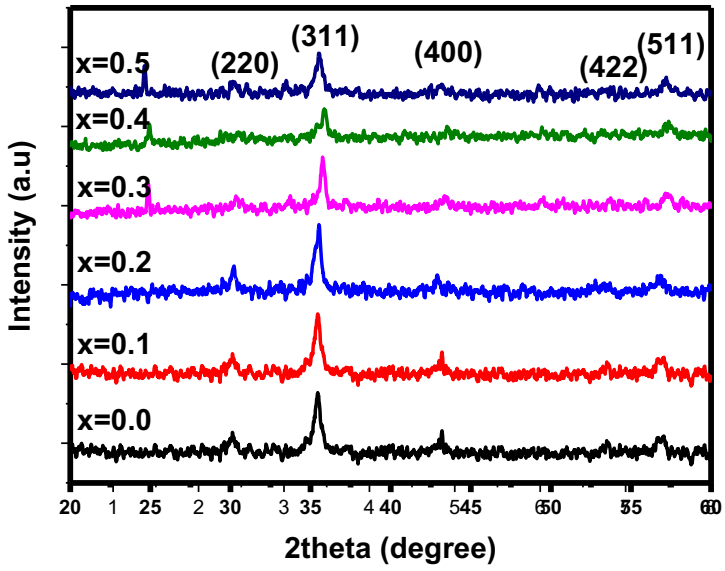

Fig. 2: XRD patterns of *CCCF-soft ferrites*

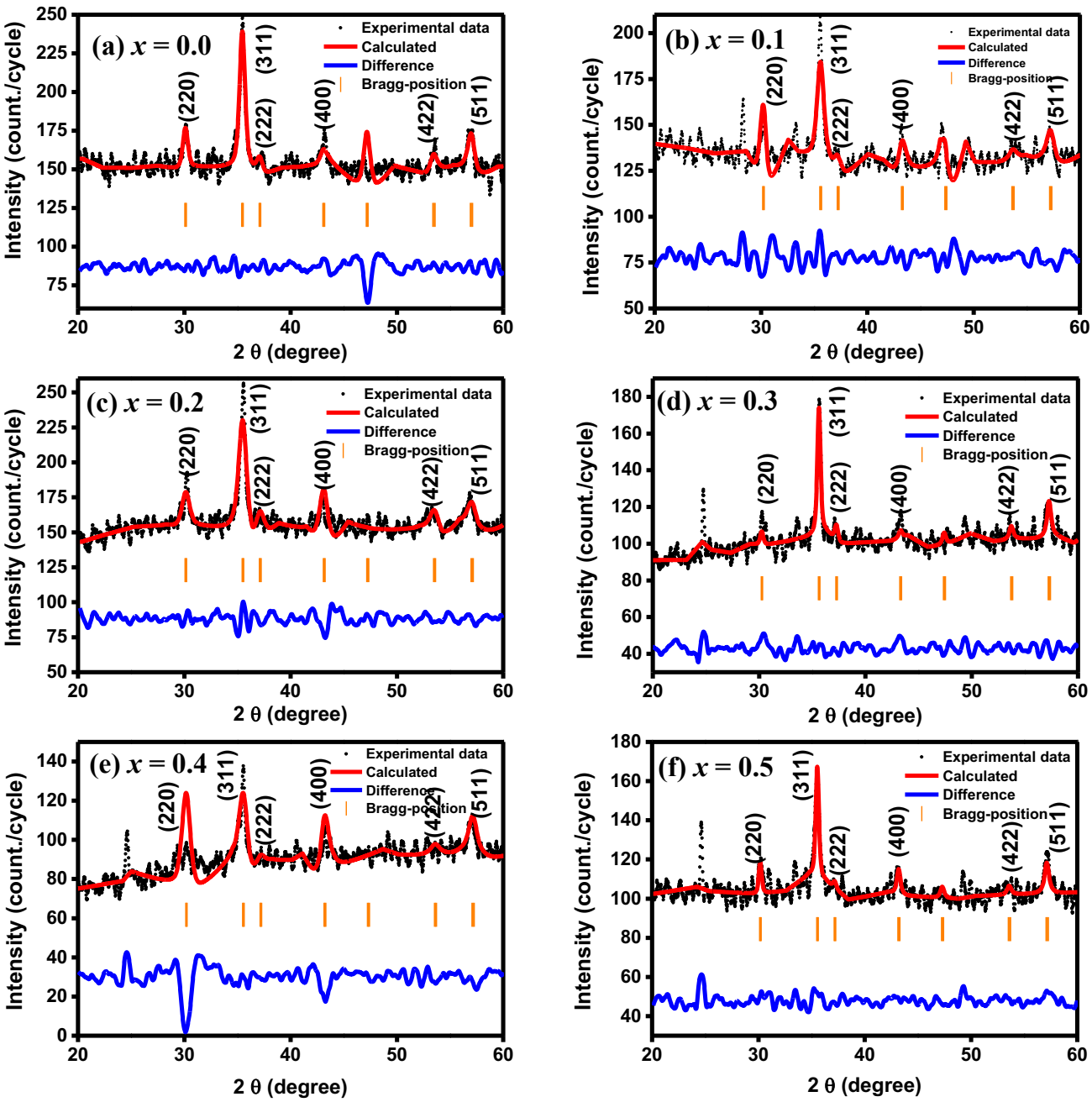

Fig. 3: Rietveld refinement for *CCCF-soft ferrites*

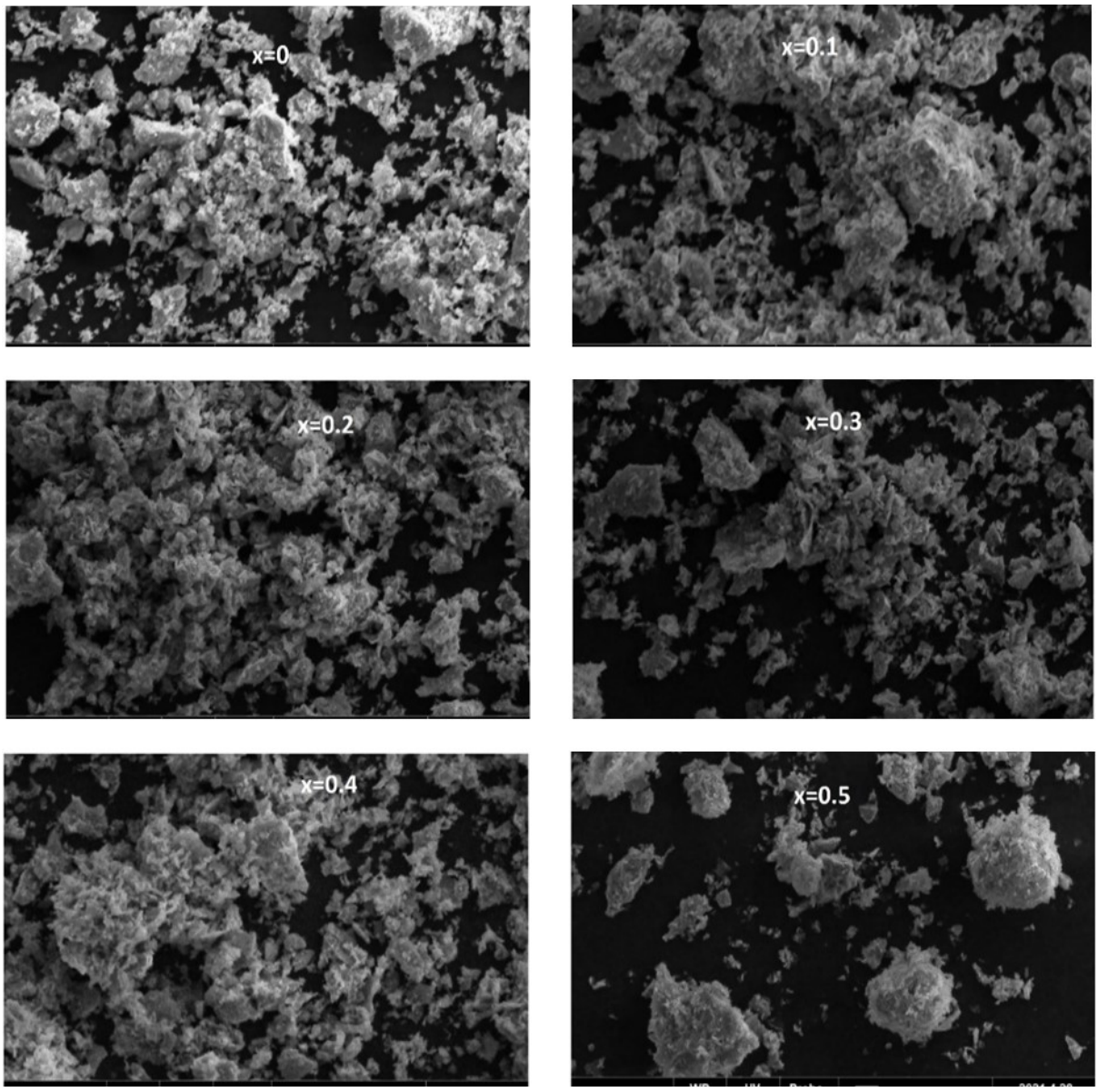

Fig. 4: SEM micrographs of *CCCF-soft ferrites*

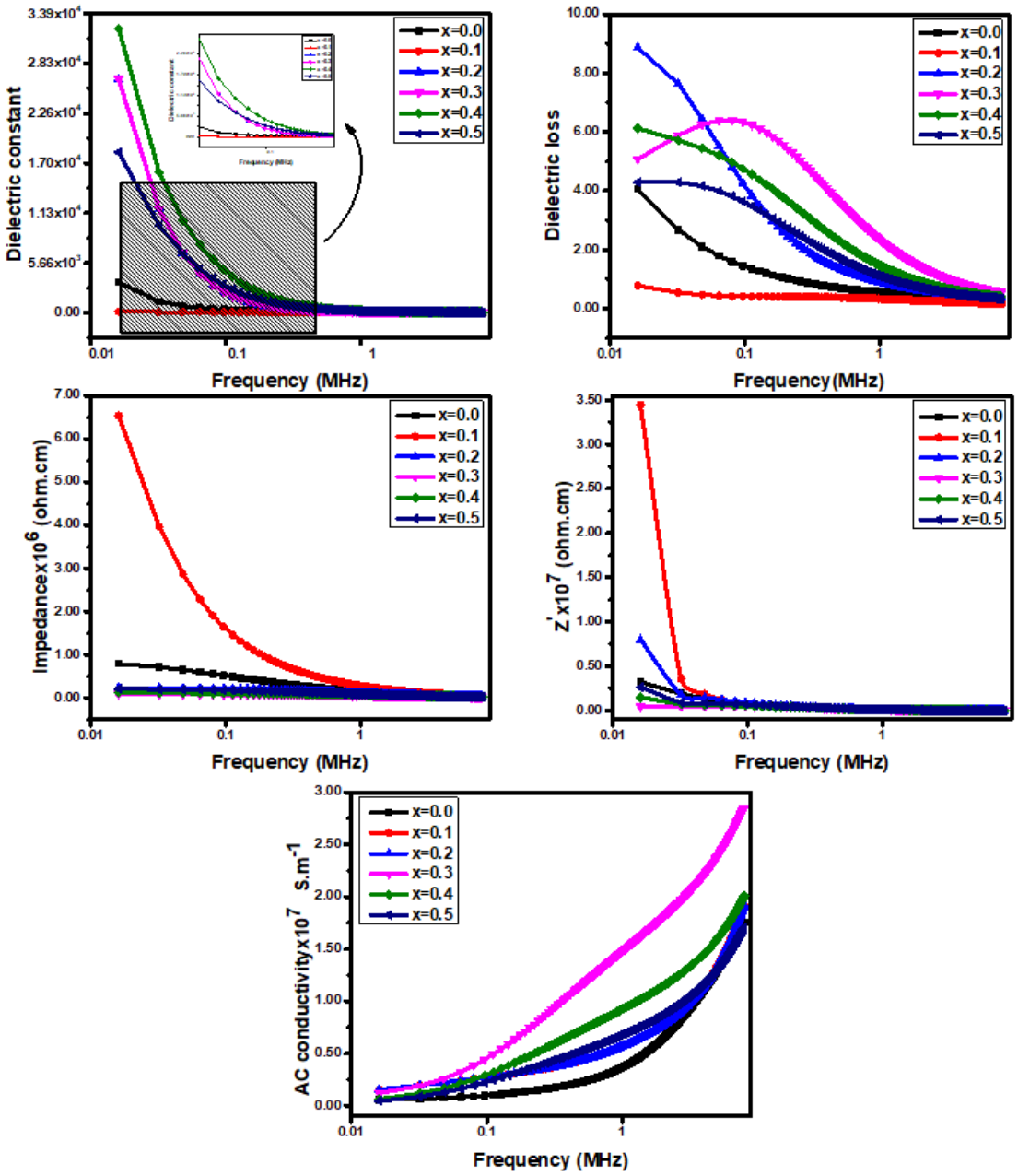

Fig. 5:Graphical representation of frequency with different dielectric parameters for *CCCF-soft ferrites*

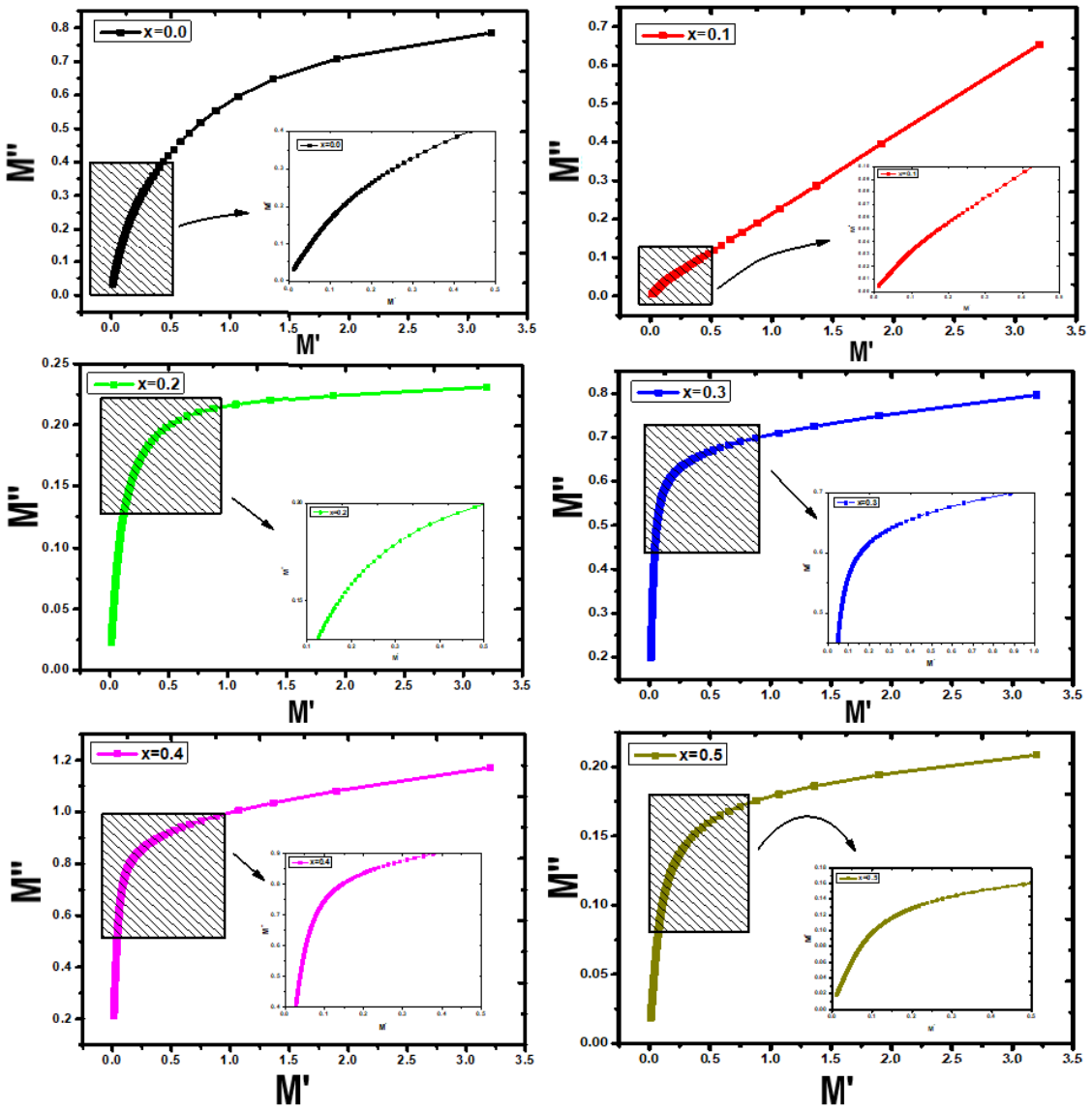

Fig. 6: Cole-Cole graph for (x=0.0, x=0.1, x=0.2, x=0.3, x=0.4 and x=0.5 for*CCCF-soft ferrites*

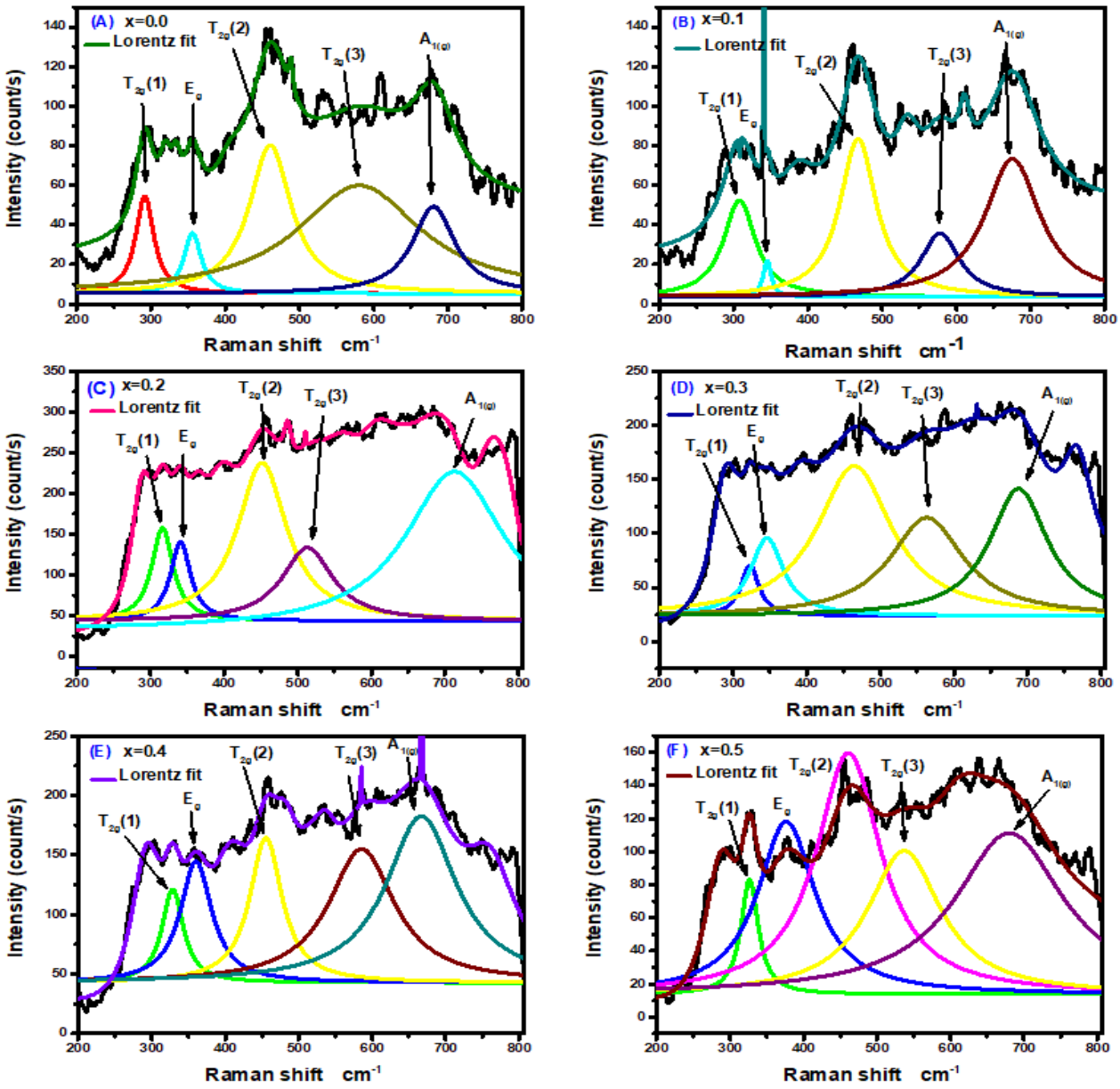

Fig. 7(A-F): Graphical representation of Raman shift and intensity along Lorentz fit for *CCCF-soft ferrites*

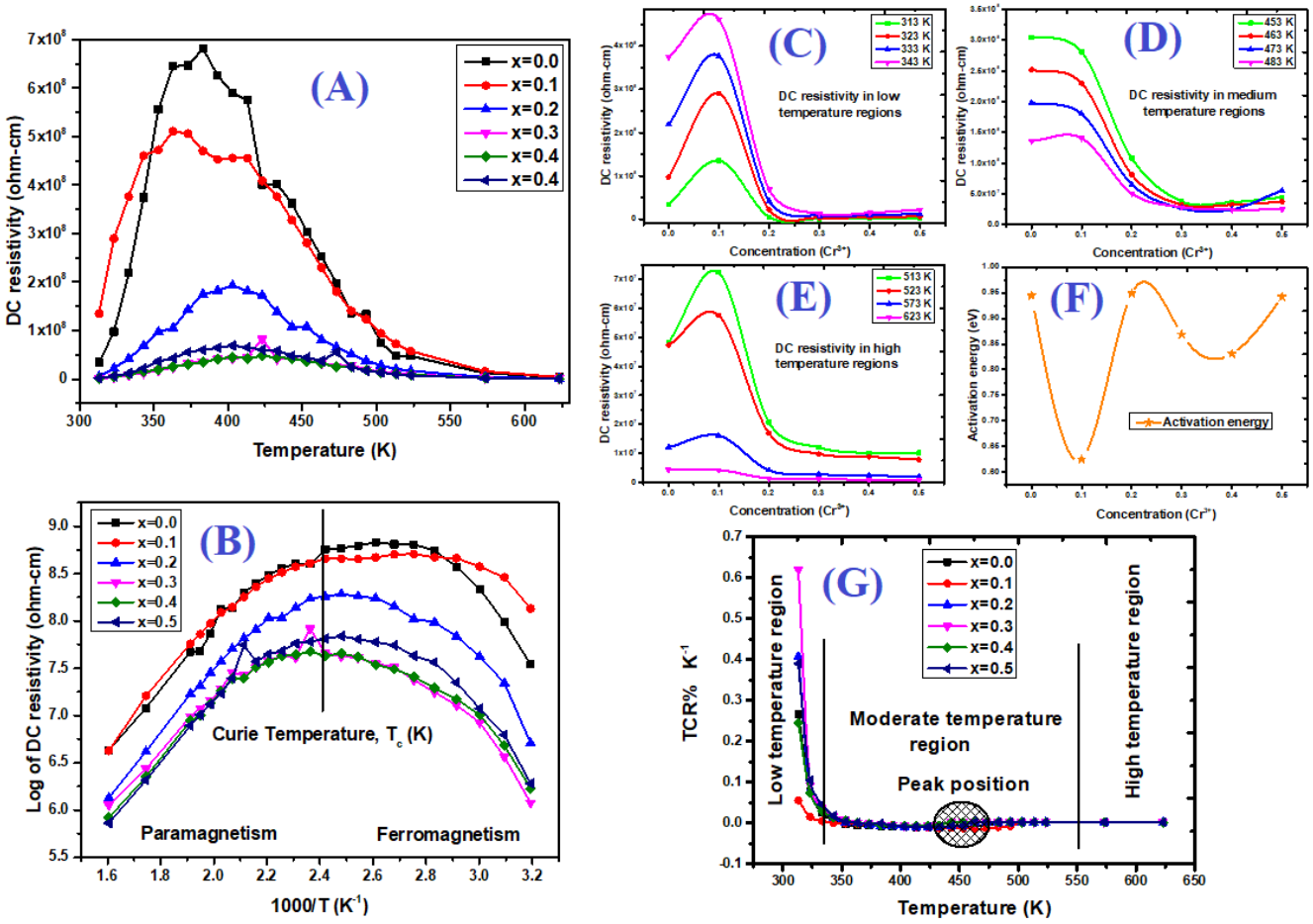

Fig. 8(A-G):(A) DC resistivity (Ω-m) with the variation of Temperature,**(B)** variation in (1000/Temperature) vs. log of resistivity (Ω-m), **(C)** DC resistivity in low temperature regions,**(D)** DC resistivity in medium temperature regions,**(E)** DC resistivity in high temperature regions, **(F)** Activation energy vs. chromium concentration, and **(G)**TCR% (K^{-1}) vs. temperature for *CCCF-soft ferrites*

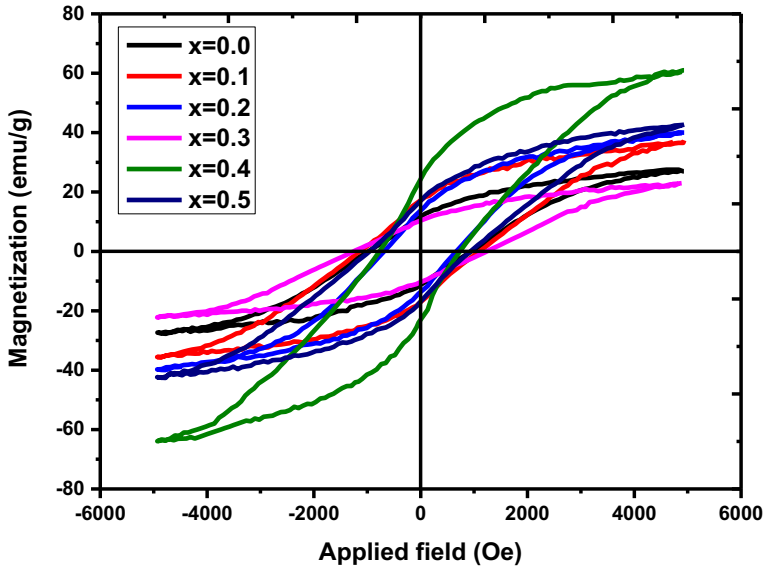

Fig. 9: Hysteresis loop of *CCCF-soft ferrites*